Solar-Terrestrial Physics. 2023. Vol. 9. Iss. 3. P. 102–111. DOI: 10.12737/stp-93202312. © 2023
D.A. Zhdanov, A.T. Altyntsev, N.S. Meshalkina, S.A. Anfinogentov. Published by INFRA-M Academic Publishing House

UDC 523.985.3, 523.985.7, 523.985-77-35
DOI: 10.12737/stp-93202312

Received May 05, 2023
Accepted August 09, 2023

STATISTICAL ANALYSIS OF MICROFLARES AS OBSERVED BY THE 4–8 GHz SPECTROPOLARIMETER

D.A. Zhdanov
Institute of Solar-Terrestrial Physics SB RAS, Irkutsk, Russia, zhdanov@iszf.irk.ru

A.T. Altyntsev
Institute of Solar-Terrestrial Physics SB RAS, Irkutsk, Russia, altyntsev@iszf.irk.ru

N.S. Meshalkina
Institute of Solar-Terrestrial Physics SB RAS, Irkutsk, Russia, nata@iszf.irk.ru

S.A. Anfinogentov
Institute of Solar-Terrestrial Physics SB RAS, Irkutsk, Russia, anfinogentov@iszf.irk.ru

Abstract. Radio observations of weak events are one of the promising methods for studying energy release and non-thermal processes in the solar corona. The development of instrumental capabilities allows for radio observations of weak transient coronal events, such as quasi-stationary brightenings and weak flares of X-ray class B and below, which were previously inaccessible for analysis. We have measured the spectral parameters of microwave radiation for thirty weak solar flares with X-ray classes ranging from A to C1.5, using observations from the Badary Broadband Microwave Spectropolarimeter (BBMS). The spectra indicate that plasma heating is caused by the appearance of non-thermal electron fluxes, which can be detected by bursts of microwave radiation, predominantly with an amplitude ~5–6 solar flux units (SFU) at 4–5 GHz frequencies. One solar flux unit (SFU) of radio emission is equal to 10–22 W/(m·Hz). The range of low-frequency spectrum growth indices f^{α} varies widely from α=0.3 to 15. The distribution of high-frequency decay indices is similar to the distributions of regular flares. One of the explanations for the appearance of large f^{α} values is the Razin effect, which can influence the shape of the gyrosynchrotron spectrum during the generation of bursts in dense plasma under relatively weak magnetic fields. We have detected two events in which the appearance of non-thermal electrons led to the generation of narrow-band bursts at frequencies near the double plasma frequency. SRH test trials have shown the potential for measuring the structure of flare sources with fluxes of the order of 1 SFU, indicating the high diagnostic potential of the radioheliograph for detecting acceleration processes in weak flare events and their localization in active regions.

Keywords: solar microwave emission, radio bursts, microflares.

INTRODUCTION

The idea of heating the solar corona with X-ray flares led researchers to the following conclusion. With increasing accuracy of experimental studies, ever-smaller-scale structures can be detected. Such terms as “microflares” and “nanoflares” have emerged in the literature; they characterize very weak manifestations of solar activity in the X-ray range [Bogachev et al., 2020]. These terms became widespread in works concerned with weak bursts in the extreme ultraviolet (EUV) range. Currently, even fainter EUV brightenings, also known as campfires, are recorded with the High-Resolution Instrument (HRI_{EUV}) [Berghmans et al., 2021].

Of the most interest is the relationship between microwaves and X-rays through electron acceleration. It has been shown, for example [Schadee et al., 1983; Qiu et al., 2004; Bogachev et al., 2020], that electron acceleration in large solar flares plays a key role in energy release and these processes manifest themselves in the same way in microflares. It is known that about half of large solar flares reveal the Neupert effect reflecting a causal relationship between the heating of flare plasma and the occurrence of electron fluxes accelerated in the impulsive phase [Neupert, 1968].

Detection of non-thermal electrons is, however, limited by the sensitivity of receiving equipment. Not many papers have been published which analyze microflares, using observations simultaneously in hard X-ray and microwave ranges [Stoiser et al., 2007; Li et al., 2022; Shibasaki et al., 1983; Chiuderi Drago et al., 1987; Gopalswamy et al., 1997; Gary et al., 1997; Nindos et al., 1999; Raulin et al., 1999; Kundu et al., 2006; Altyntsev et al., 2020a; Battaglia et al., 2021].

Qiu et al. [2004] have reported statistically significant results of analysis of microflares, using data obtained in two ranges: RHESSI (Ramaty High Energy Solar Spectroscopic Imager) observations in the hard X-ray range [Lin et al., 2002] and OVSA (Owens Valley Solar Array) observations in the microwave range [Gary, Hurford, 1990]. Microflares for the analysis were selected by a signal in a 12–25 keV X-ray channel whose value should not exceed 100 counts per second. For joint analysis, 56 events have been chosen which correspond to X-ray flares of class no higher than C1.0 according to GOES.

Large OVSA antennas measured microwave fluxes with an intensity of 0.2 SFU. Shapes of the microwave spectra observed were specific to the gyrosynchrotron emission mechanism. The frequencies of maximum spectra were ~6 GHz, and the intensity was below 10 SFU. The main purpose of the analysis was to determine the charac-

teristics of non-thermal electrons accelerated in weak events.

It is known that in the case of gyrosynchrotron spectrum at frequencies above the maximum-spectrum frequency f_{max}, the decay rate of the microwave spectrum β (high-frequency spectral slope, or high-frequency slope) is determined by the power-law index of δ-energy distribution of non-thermal electrons [Dulk, Marsh, 1982]. Qiu et al. [2004] have estimated the power-law index of non-thermal electrons within δ=2÷4.

Characteristics of the low-frequency spectral slope were not discussed in that study. Nevertheless, under the gyrosynchrotron emission mechanism the low-frequency part also depends on the distribution of non-thermal electrons. In this case, the dependence of the slope on δ is much weaker and proportional to the radio flux intensity $S \sim f^{\alpha}$. For example, in a uniform source for δ=2÷7 the slope is limited to α=2.67÷3.1 [Shaik, Gary, 2021]. In the actually observed spectra, the range of α variations is, however, much wider. So, in [Stahli et al., 1989], in which the spectrum was observed with a sufficiently high spectral resolution, α was shown to vary from 1 to 10 and the region near α=3 is weakly distinguished by the frequency of occurrence in flare bursts. The appearance of sloping spectra with α<2.6 was interpreted as nonuniformity of the microwave source, i.e. the presence of emitting regions with weaker magnetic fields.

To interpret spectra with steep slopes α>3.1, several effects have been proposed which are associated both with peculiarities of emission generation in a source and with external factors [Stahli et al., 1989]. For example, the Razin effect is most often used to explain large values of α — suppression of gyrosynchrotron emission in dense plasma with density n at frequencies $f_R < 20\ n/B$, where B is the magnetic field in a source [Ginzburg, Syrovatskii, 1965]. In this case, deformation of the low-frequency spectrum can be used to estimate the plasma density in a gyrosynchrotron emission source (see, e.g., [Ramaty, 1969; Fleishman, Kuznetsov, 2010]).

Weak transient events in the microwave range are primarily linked to fine temporal and spectral structures of microwave-burst emission. Sources of fine-structure emission are known to not always coincide with sources of broadband continuous emission of microwave bursts. This is due to different requirements for the conditions of occurrence and output of emission in different emission generation mechanisms. It has been shown that a fine structure can be observed without an accompanying microwave burst [Zhdanov, Zandanov, 2015]. The absence of a source of shielding continuum emission makes such events especially interesting. Firstly, the accuracy of localization of a fine-structure emission source increases; secondly, the degree of interpretation ambiguity and the relationship between observations in different emission bands decreases.

On the other hand, the first multi-wave SRH observations [Altyntsev et al., 2020b] have shown that along with gyrosynchrotron emission, the occurrence of non-thermal electrons in microflares can be detected from coherent narrowband emission of non-thermal electrons trapped in low magnetic loops with a sufficiently high density [Altyntsev et al., 2022; Altyntsev et al., 2023]. Yet, weak transient events in the microwave range are most often not associated with the fine structure of microwave emission or coherent emission mechanisms since they are not so extraordinary.

The purpose of this work is to obtain new experimental results confirming the role of accelerated electrons in plasma heating in weak flares during low solar activity of the new cycle by analyzing microwave observations with high frequency resolution and high flux sensitivity. Analysis of combined microwave observations made with the Badary Broadband Microwave Spectropolarimeter (BBMS) 4–8 GHz [Zhdanov, Zandanov, 2011] and using SRH multi-wave imaging data has allowed us to find 30 weak events identified as microwave microflares. The observations were carried out during low solar activity in April–December 2021, which contributed to the detection of sufficiently weak microwave responses against the background of integral solar emission, which corresponded to X-ray flares of classes A to C2.0 according to the GOES classification.

INSTRUMENTS AND EVENT SELECTION

The work is based on BBMS data with a time resolution of 1 s. In this mode, the flux sensitivity of the receiver is about 1 SFU. The spectral resolution of the data allows us to find the peak frequency f_{max}, the maximum flux S_{max}, and spectral slopes α and β of microwave bursts provided that the peak frequency is within 4–8 GHz. In exceptional cases, to determine the shape of the microwave spectrum at frequencies below 4 GHz, we have used data from the 2–24 GHz Solar Radio Spectropolarimeter (SRS, [Muratov, 2011]). For f_{max}>8 GHz, we have employed data from Nobeyama Radio Polarimeter (NORP) at 9.4 and 17 GHz.

In the simplest case, the parameters of microwave spectra S_{max}, f_{max}, α, β can be found by approximating the spectrum by a power-law function, assuming that emission comes from a uniform gyrosynchrotron source. The spectrum $S(f)$ was approximated by power-law function (1) having a form with a single frequency maximum and power-law slopes at low and high frequencies [Stahli et al., 1989]:

$$S = Af^{a}\left(1 - e^{Bf^{-b}}\right), \quad (1)$$

where f is the frequency; A, B, a, b are free parameters. The parameter a corresponds to the low-frequency spectral slope α, and the high-frequency spectral slope is determined by the expression β=(a–b).

Analysis of 80 events from the BBMS catalog has revealed that 45 events occurred during X-ray flares of class no higher than C2.0 according to GOES. The threshold of C2.0 was chosen arbitrarily to limit the size of the initial sample of events. The spectra were approximated at T_{max}, when the radio flux reached the maximum value S_{max}. Table presents 30 events for which all S_{max}, f_{max}, α, β have been found.

Figure 1, *a* illustrates a case when the result of approximation of the microwave spectrum in the September

Summary of events

No.	DATE	T_{max}	$\Delta\tau$, s	ΔGOES	GOES	S_{max}	f_{max}	α	β	SRH	HXR
			сек	вт/м^2		с.е.п.	ГГц				
1	2021-04-19	06:29:59	–16	3.5×10^{-8}	B2.1	1.06	5.71	2.15	–4.60	3–6	S/10
2	2021-04-21	01:27:48	–4	1.3×10^{-6}	C1.8	4.95	5.13	2.20	–2.47	3–6	no
3	2021-05-09	04:34:41	5	1.5×10^{-6}	C1.7	7.52	5.13	2.51	–3.00	3–6	F/50
4	2021-05-11	03:19:45	8	9.0×10^{-8}	B1.7	6.07	4.51	1.30	–2.20	3–6	S/10
5	2021-05-22	01:24:36	–7	9.5×10^{-8}	B2.9	3.23	5.54	6.86	–0.39	3–6	S/25
6	2021-05-23	01:38:31	–14	2.9×10^{-7}	B6.0	2.26	4.68	4.18	–2.80	3–6	S/15
7	2021-05-27	03:09:40	92	1.1×10^{-6}	C1.4	8.39	7.22	4.26	–0.66	3–6	S/no
8	2021-05-27	03:19:57	–12	7.6×10^{-8}	C1.1	4.10	6.27	4.17	–2.17	3–6	S/no
9	2021-05-27	04:41:38	–53	3.4×10^{-7}	B6.0	4.19	7.90	3.40	–0.65	3–6	S/no
10	2021-05-27	06:46:23	2	5.9×10^{-7}	B9.2	4.06	6.35	6.41	–0.58	–	no
11	2021-05-27	08:06:59	–16	7.4×10^{-7}	C1.0	5.15	8.77	4.07	–0.43	3–6	no
12	2021-06-03	01:36:26	0	5.2×10^{-8}	B1.2	4.91	5.81	3.64	–1.61	3–6	no
13	2021-08-22	01:04:09	–10	1.2×10^{-7}	B4.2	3.39	5.31	4.19	–3.45	3–6	S/25
14	2021-08-22	04:12:40	–23	1.0×10^{-6}	C1.2	6.74	4.42	1.25	–6.76	3–6	F/25 S/25
15	2021-08-22	08:30:30	13	3.3×10^{-7}	B5.5	3.43	5.80	1.29	–4.10	3–6	F/50 S/25
16	2021-08-30	09:34:35	–5	6.6×10^{-7}	C1.1	5.69	7.49	1.13	–3.00	3–6	S/25
17	2021-09-06	05:57:55	3	1.5×10^{-7}	B5.5	4.90	3.81	2.24	–2.30	3–6	F/25 S25
18	2021-09-11	06:20:24	9	2.9×10^{-8}	B3.5	4.05	5.36	6.10	–1.51	3–6	F/100 S/25
19	2021-09-13	02:55:54	1	4.5×10^{-7}	B8.6	11.1	5.51	3.24	–3.11	3–6	S/25
20	2021-09-21	05:36:53	10	2.7×10^{-9}	B2.6	no	no	1.99	no	3–6	F/50 S/no
21	2021-09-22	03:23:30	16	2.1×10^{-7}	B3.2	4.41	4.54	9.67	–0.70	3–6	S/no
22	2021-09-25	06:12:57	2	7.6×10^{-8}	B3.3	14.8	4.27	9.04	–7.43	3–6	S/25
23	2021-10-30	05:26:06	–16	2.5×10^{-7}	B6.5	3.43	5.40	2.26	–2.00	–	S/25
24	2021-10-31	03:22:28	1	4.9×10^{-7}	C1.8	8.40	6.77	1.56	–3.80	–	S/no
25	2021-12-15	03:44:29	5	6.0×10^{-7}	C2.0	10.8	13.5	3.30	–0.58	6–12	F/25 S/25
26	2021-12-16	07:47:05	12	3.2×10^{-7}	B9.8	9.69	5.75	4.05	–2.20	6–12	F/50 S/25
27	2021-12-17	04:39:07	7	6.5×10^{-8}	B8.9	10.3	4.60	15.10	–0.58	6–12	S/25
28	2021-12-20	05:50:12	–18	1.2×10^{-7}	B9.1	5.60	3.83	8.38	–14.00	6–12	F/50 S/25
29	2021-12-23	04:39:35	95	2.0×10^{-7}	C1.3	2.74	5.63	0.604	–4.38	6–12	F/50 S/10
30	2021-12-23	06:20:30	309	1.2×10^{-7}	C1.4	1.97	5.01	0.34	–5.10	6–12	S/25

21, 2021 event cannot be used for the analysis. In the range 4–8 GHz, the radio flux is seen to monotonically increase with frequency and, in order to determine the peak frequency, we have to use data from Nobeyama polarimeters at 9.4 and 17 GHz. Yet, the sensitivity of the polarimeter receiver at 9.4 GHz did not allow us to detect a burst above the background emission. In Figure 1, the height of vertical segments corresponds to the 3σ standard deviation, calculated before the burst. Thus, there are no reliable points in the high-frequency spectrum of this event, thereby making it impossible to find f_{max}, and hence S_{max} and β. In this event, we can estimate only the α slope. In the remaining 15 events, which are not included in the final table, there were similar ambiguities in the approximation.

Scheme of the approximation is given in Figure 1, *b*. In the September 25, 2021 event, for instance, the spectral peak was at a frequency of 4.3 GHz, the maximum flux reached 14.8 SFU, and the spectral slopes $\alpha\approx9.0$ and $\beta\approx-7.4$.

Spatial information about the microwave emission sources is available from SRH test observations in the mode when only one of three antenna arrays is working. From April to October, the events were recorded by the 3–6 GHz antenna array. From November to December, six events were recorded during the 6–12 GHz array test trials; no observations were made during three events. The observation mode is shown in Table.

Figure 2, *a* depicts the relationship between the observations: GOES time profiles of soft X-rays in the 1–8 Å channel and the derivative of this profile during a microflare on September 25, 2021. In the growth phase of soft X-rays of a B3.4 flare, a 20 s microwave burst was observed.

Panels *b*, *c* show time profiles of the flux at six SRH frequencies from the 3–6 GHz array: 2.8, 3.1, 3.4, 3.9, 4.7, and 5.6 GHz. Sensitivity of the 3–6 GHz 129-antenna array of SRH is by an order of magnitude higher

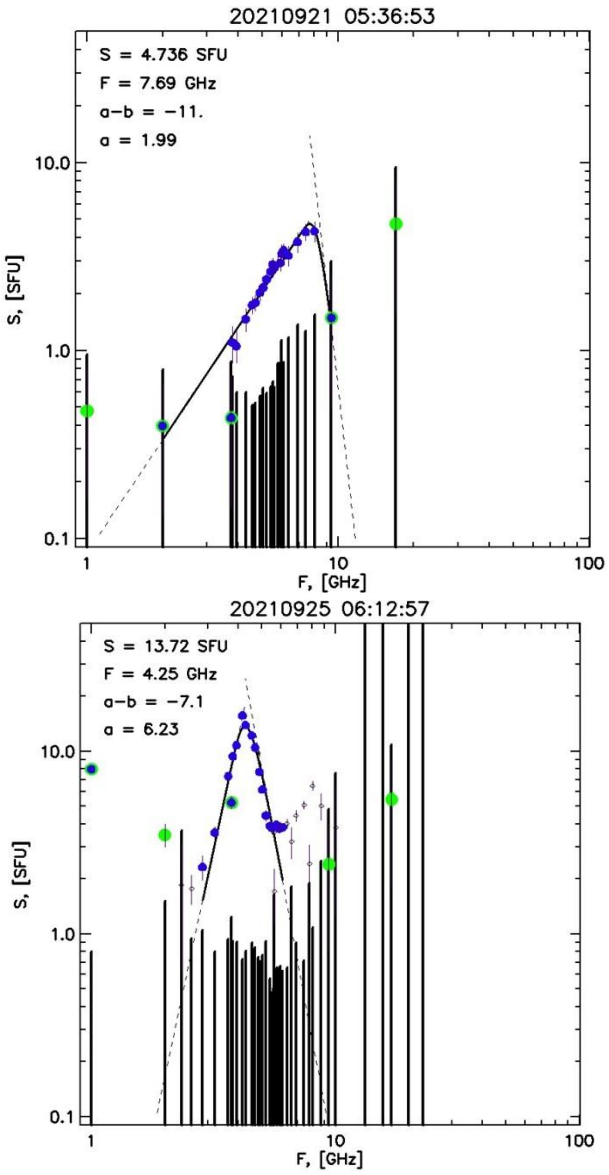

Figure 1. Approximation of microwave spectra. Blue dots mark BBMS data; green dots, Nobeyama polarimeter data. Result of data approximation is indicated by a solid curve; dashed lines are asymptotes of spectral slopes; vertical segments are 3σ standard errors for each frequency, which were calculated before the burst. Approximation of September 21, 2021 event No. 20 (panel *a*). The flux at a frequency of 9.4 GHz is below the background 3σ standard error. In this case, β, S_{max}, and f_{max} are undefined, whereas α is defined. Approximation of September 25, 2021 event No. 22 (panel *b*)

than that of BBMS. Noise track in the SRH flux curves is almost invisible, i.e. the flux sensitivity of the radioheliograph is higher than 10 % of 1 SFU. In panel *d* are signals from three channels of hard X-rays with energies from 4 to 25 keV.

In Table, a soft X-ray increase ΔGOES and flare GOES-class are determined for each event. The time shift Δτ is found from the difference between the moment of X-ray profile derivative maximum and the moment of maximum microwave flux T_{max} (see Figure 2). As noted above, the relationship between hard and soft X-rays manifests itself through the Neupert effect, which is determined from the derivative of soft X-rays.

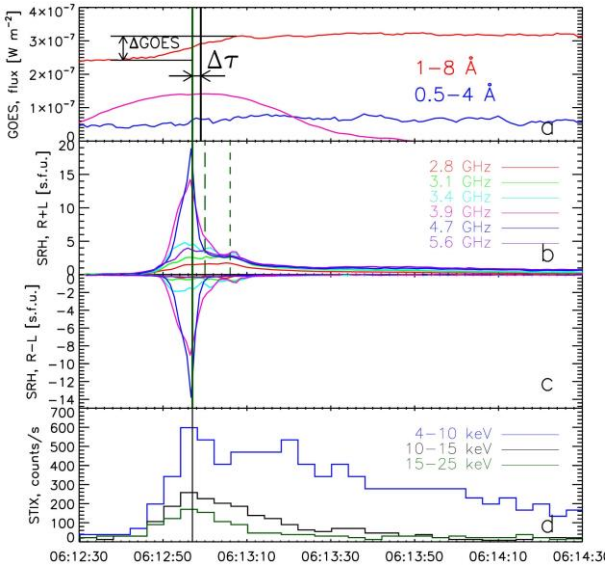

Figure 2. The September 25, 2021 event: time profiles of GOES soft X-rays (blue and red curves) and a 1–8 Å profile derivative (pink curve), whose maxima are marked with black vertical lines, ΔGOES is an increase in soft X-rays, Δτ is a shift between burst maxima and GOES derivative (*a*); profiles of microwave flux in intensity (R+L) and polarization (R–L) recorded by SRH at six frequencies; green vertical lines are maxima of the microwave burst (solid line) and sub-peaks (dashed line) (*b*,*c*); profiles of hard X-rays of the STIX spectrometer (*d*)

The last column contains information on hard X-rays for each event, the F index marks FERMI/GBM observations [Meegan et al., 2009]; the S index, observations with Spectrometer Telescope for Imaging X-rays (STIX, [Krucker et al., 2020; Xiao et al., 2023]). The responses are generally observed in channels with an energy to 25 keV. There are no hard X-ray observations for four events. From the differences between time profiles at different frequencies it follows that the burst spectrum varied over time: at 3.9 and 4.7 GHz there was a narrowband intense burst with a half-height duration of 3.2 s. During the entire burst, emission has left circular polarization whose degree depends on the receiving frequency. Typically it does not exceed 20 %, but increases sharply at 3.9 and 4.7 GHz, reaching 70 % during a narrowband burst. During the burst, an intensity increase ΔGOES corresponded to $7.6 \cdot 10^{-8}$ W/m^2 or GOES-level A7.6. The delay of the derivative of the 1–8 Å profile relative to maximum microwave burst Δτ≈2 s. To identify the main growth phase, the GOES signal was smoothed with a window of 2 min before differentiation.

In the GOES 0.5–4 Å channel, the response to this flare was long, but its magnitude was at the noise level. In hard X-rays, the moments of maximum fluxes coincide with maximum microwave emission. In a channel with a low energy 4–10 keV, the duration of a burst exceeds 1 min, which is much longer than the duration of a burst in microwaves. In the 10–25 keV channels, the flux curves are close in shape and duration to the microwave profiles at 3.4 and 5.6 GHz, at which a short intense burst at intermediate frequencies does not show up.

Figure 3 presents microwave emission spectra of the September 25, 2021 burst, which were measured at three time points, marked in Figure 2, *b*. Background emission of the solar disk is excluded owing to the level before the burst. The solid curve shows the approximation of the BBMS spectrum at the burst peak by Formula (1), used to determine spectrum parameters and to calibrate the amplitude of SRH measurements. During the short burst, the flux intensity at ~4.5 GHz increases more than fourfold for 5 s, and the band of emitted frequencies at the half-height of the spectrum decreases to ~2 GHz. During the two following moments, the spectra marked with rhombuses and triangles are much wider.

STATISTICAL PROPERTIES OF THE SAMPLE OF BURSTS

Distributions of the microwave bursts, listed in Table, by amplitude and frequency of spectrum maximum are illustrated in Figure 4. Histograms of our sample of events with fluxes to 15 SFU are depicted by solid lines in comparison with the sample [Stahli et al., 1989] that includes bursts with fluxes ranging from 3 to 620 SFU (dashed lines). Our sample for weak events has more bursts with lower frequencies of maximum spectra 5–6 GHz (*a*) and amplitudes ~4–5 SFU (*b*).

The relationship of flare plasma heating with intensity of radio emission fluxes, generated by non-thermal electrons, is shown in Figure 5, *a*. The spread of ΔGOES relative to the amplitude of microwave emission *S* is very wide and can reach two orders of magnitude. That said, there is a limitation of maximum ΔGOES, which do not exceed $4 \cdot 10^{-8} (S_{max})^2$ (dashed line).

Figure 5, *b* presents a histogram of events over the delay Δτ determined by the difference between the moment of soft X-ray derivative maximum and the moment of microwave burst maximum.

It is well known that about half of large solar flares exhibit the Neupert effect reflecting the causal relationship between flare plasma heating and the appearance of electron flux accelerated in the impulsive phase [Neupert, 1968]. We have therefore used the soft X-ray derivative to determine the estimated maximum moment of electron injection. We can see from the distribution that in most events the Δτ modulus does not exceed 20 s.

This fact may point to the relationship between the observed microwave bursts and their associated X-ray bursts.

The values Δτ>50 s have been observed in four cases. Note that for event No. 30 in Figure 5, *b* the extreme value Δτ=309 s is not indicated.

Figure 6 presents histograms of spectral slopes α and β and the ratio between them (right panel). We have compared them with those obtained by other authors.

The low-frequency slope α was compared with the results of [Stahli et al., 1989]. We take the range of α variation for a uniform source from 2.67 to 3.1 as a unit step

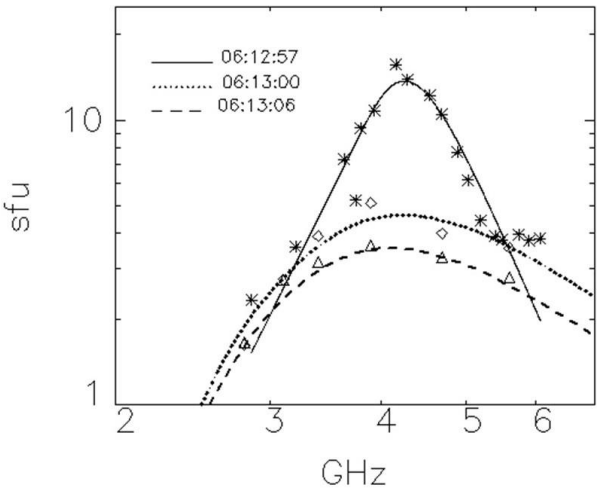

Figure 3. September 25, 2021 event. Microwave spectra at the time points marked in Figure 2, *b*. The solid curve is approximation by Formula (1) of the BBMS spectrum (asterisks) at the burst maximum. SRH measurements in subsequent moments are indicated by rhombuses and triangles. Dotted and dashed curves show the results of approximation of the measured sub-peak spectra by gyrosynchrotron emission

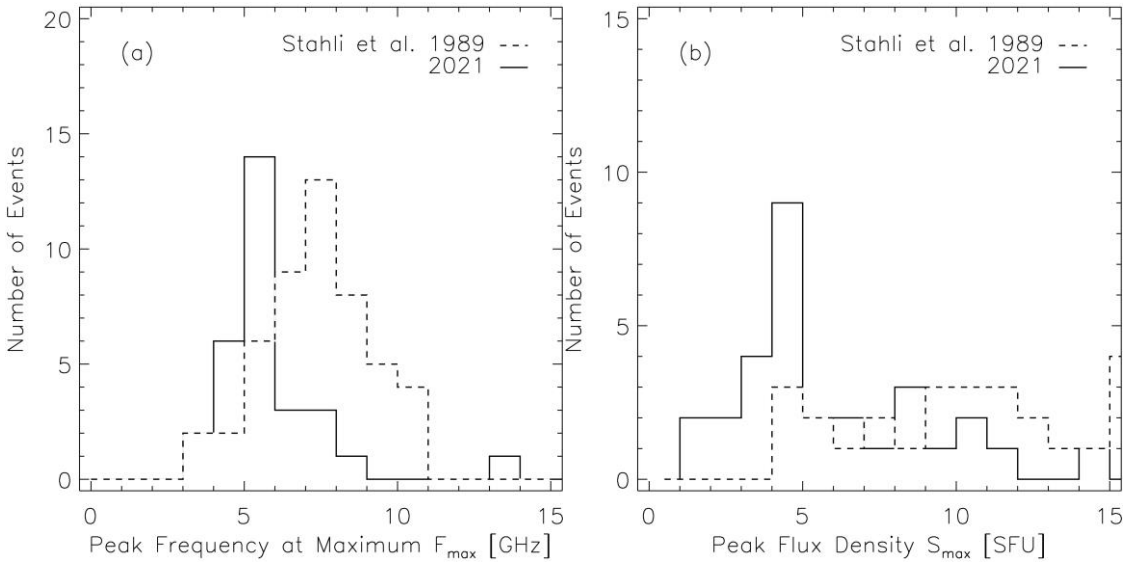

Figure 4. Distribution of bursts over frequency (*a*) and amplitude (*b*). The dashed line shows similar dependencies from [Stahli et al., 1989]

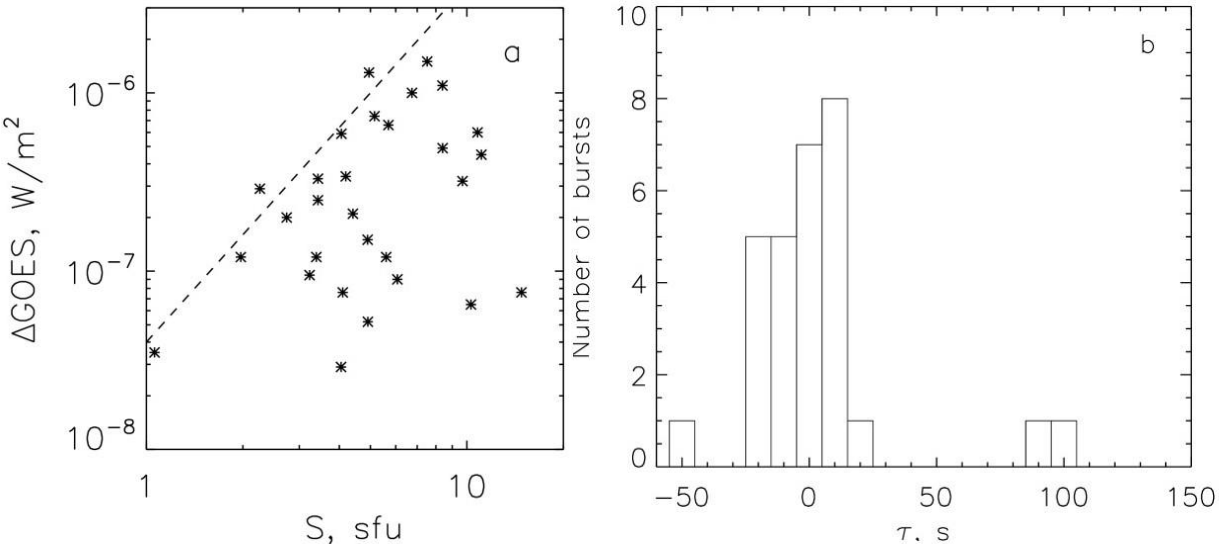

Figure 5. ΔGOES as function of microwave spectrum amplitude (*a*), distribution of events over delays τ of soft X-ray derivative maximum as function of microwave burst maximum (*b*)

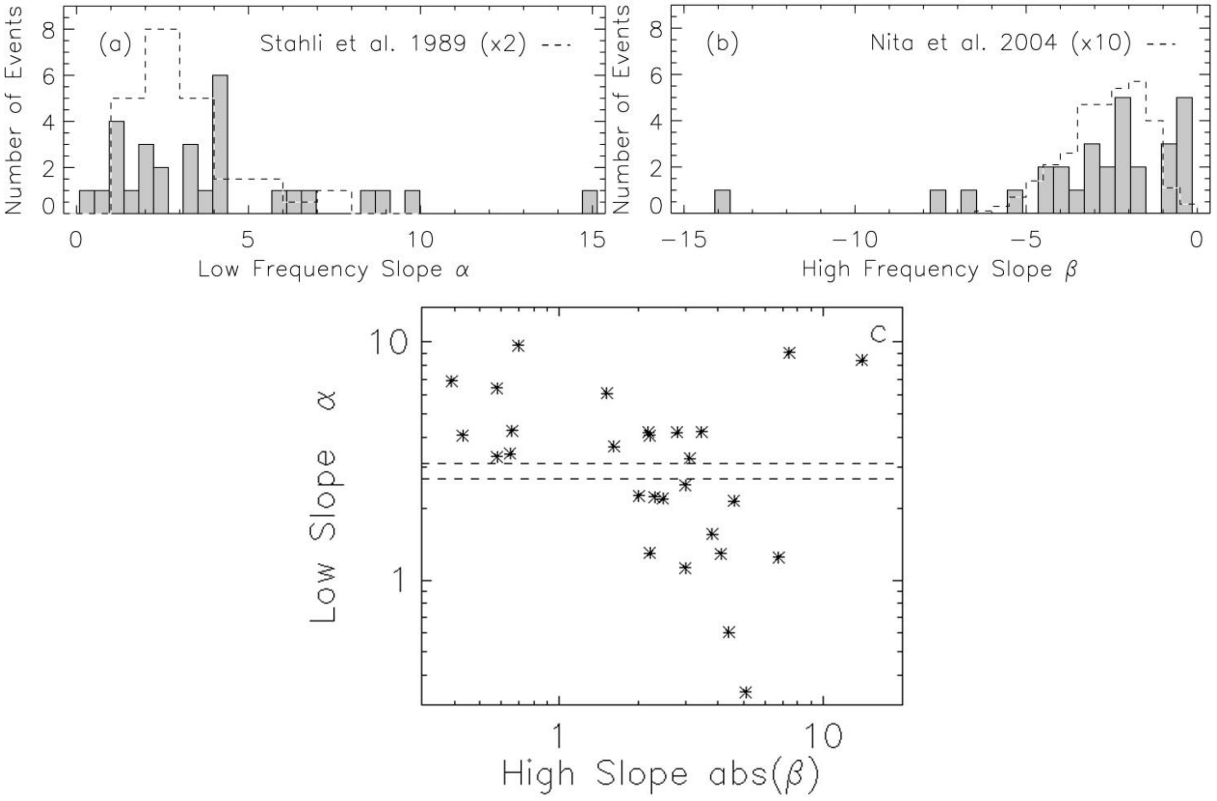

Figure 6. Histograms of low-frequency (*a*) and high-frequency (*b*) spectral slopes and the relationship between these slopes (*c*). Horizontal lines correspond to α=2.67 and 3.1. Histograms for the burst sample collected by Stahli et al. [1989] are shown by dashed lines at a scale of 1:2; for the β sample obtained by Nita et al. [2004], at a scale of 1:10

interval of the histogram. There is a wide spread of α values; a similar result was obtained in [Stahli et al., 1989]. Yet, the range of values corresponding to the gyrosynchrotron mechanism of emission from a uniform source, unlike the sample collected in [Stahli et al., 1989], is not distinguished by the frequency of recorded events. The occurrence of events with α<2.6 is naturally associated with violations of the uniformity of the emission source. In weak events, a simple configuration and small sources can be expected, and the percentage of events with a complex structure (>30 %) is relatively low. In other events, the low-frequency spectral slope α>3.1, i.e. steeper than expected for gyrosynchrotron emission.

For the high-frequency part of the β spectrum, we have compared with the results obtained by Nita et al. [2004]. For most bursts of our sample, |β|≤7.

It is usually assumed that the steep spectral slope at frequencies below maximum is caused by the Razin effect — suppression of gyrosynchrotron emission by dense background plasma, which may be peculiar to

sources of weak flares with low heights [Ramaty, 1969; Fleishman, Kuznetsov, 2010]. The relationship between α and β is consistent with this assumption (see Figure 6, *c*). In the case of the Razin effect, the gyrosynchrotron spectrum is modified as follows: at low frequencies, the spectral slope becomes great, and the magnitude of the flux at spectral peak decreases, and hence the spectral slope at high frequencies becomes gentler. A similar behavior is observed in observations: in Figure 6, *c*, to large β values correspond small absolute α values. In panel *c*, two flares stand out in the spectra of which both slopes are abnormally steep (two asterisks in the top right corner). To study features of bursts No. 22 and 28, we have used spatially-resolved SRH observations. Observations of event No. 28 with SRH were made by the 6–12 GHz antenna array; and, as observed by the 4–8 GHz spectropolarimeter, the frequency of the maximum spectrum was near 3.8 GHz. We will therefore focus on event No. 22, namely, the September 25, 2021 burst.

SEPTEMBER 25, 2021 BURST

The microwave burst of event No. 22 occurred in active region 12871, located in the southern hemisphere near the central meridian, on September 25, 2021 between 06:12 and 06:14 UT during an increase in X-rays to the A7.6 level. Figure 7 illustrates the emergence of a bright loop during an X-ray flare observed in the 131 Å high-temperature line.

At the peak of the microwave burst, the spectrum had a steep slope at both low (α≈9) and high (β≈–7.4) frequencies. The burst can be classified as narrowband since it had a frequency band no more than 2 GHz and was observed at frequencies from 3.2 to 5.2 GHz. Such values of slope and bandwidth do not fit into the standard model of uniform gyrosynchrotron source.

On the other hand, due to the high sensitivity of SRH in the spectrometric observation mode, two more sub-peaks were identified in the total flux time profile at several frequencies during the decay phase after the main peak (see Figure 2, *b*). Spectra of these sub-peaks are much flatter (see Figure 3). This fact may suggest both that the emission generation parameters change and emission comes from another source. To make this information more accurate, we have used SRH spatial observations.

The microwave emission source (R+L) is shown by white contours at the 0.3, 0.5, and 0.9 levels of maximum brightness temperature (Figure 7). The imaging time 06:12:57 corresponds to the peak of the narrowband intense burst. Note that during observation of this event, eight antennas of the central antenna array were switched off. This does not affect measurements of the spatial structure of compact sources, but has an effect on the brightness distribution of large-scale extended sources such as the solar disk. Therefore, radio maps at different frequencies were aligned not by the disk, but by a remote gyroresonance source in the northern part of the Sun. When combining EUV images with SRH radio maps, we have found that a bright UV loop is located close to the center of the radio source brightness.

Dimensions of the burst source decrease with increasing frequency. At high frequencies, the shape of the isoline is at the level of 0.5 and its size become close to the size of the SRH diagram (yellow oval). To the narrowband burst correspond images at 3.9 and 4.7 GHz; at these frequencies, the size of the microwave source across the diagram and along the UV loop was ~20″. At other frequencies, the brightness temperature of the flare source is much lower; and at 0.3 and 0.5 isolines, the presence of quasi-stationary sources is already noticeable. Therefore, the region covered by the isolines at low frequencies is expanding, and a new source appears in images at 5.6 GHz.

The brightness temperature isolines in polarization at the level of 0.5 from maximum are close to similar isolines in intensity. In accordance with the behavior of the time profiles in Figure 2, *c*, polarization at all frequencies is negative, i.e. corresponds to left circular polarization, but the polarization degree depends on frequency. At 3.9 and 4.7 GHz, it was higher than 60 %.

DISCUSSION

The low level of activity during the SRH test observations allowed us to select 30 weak microwave bursts during flares with a soft X-ray increase ΔGOES less than $1.5 \cdot 10^{-6}$ W/m^2 for the analysis, using the multi-wave spectropolarimeter BBMS.

Statistical analysis has shown that microwave bursts generally occur at the X-ray growth front. Thus, the conclusion made in [Lysenko et al., 2018; Altyntsev et al., 2020a] that weak flares are often impulsive and the energy release of such flares is dominated by electron acceleration at the initial stage is confirmed. This behavior is typical of strong impulsive flares and is called the Neupert effect [Neupert, 1968]. In the sample we analyzed, the X-ray increase ΔGOES was observed within three orders of magnitude from $2.7 \cdot 10^{-9}$ to $1.5 \cdot 10^{-6}$W/m^2. The relationship of ΔGOES with the burst amplitude S_{max} turned out to be weak, but a restriction to the maximum value of ΔGOES [W/m^2] $< 4 \cdot 10^{-8} (S_{max})^2$ was found.

The parameters of microwave spectra listed in Table are characteristic of gyrosynchrotron emission of medium-relativistic electrons. Nonetheless, the observed distribution of the low-frequency spectral slope α does not fit the model in which the optically thick part of the spectrum is controlled by absorption of gyrosynchrotron emission by the same non-thermal electrons that are responsible for the high-frequency emission. Cases with α<2.6 can be realized due to the nonuniformity of the source, for example, due to adding flare regions with weaker magnetic fields at low emission frequencies. Various effects that lead to the occurrence of bursts with α>3.1 are discussed in [Stahli et al., 1989]. In our sample, the main effect seems to be the Razin absorption since in this case there is a link between α and β (see Figure 6, *c*), which manifests itself in the fact that to steeper spectral slopes at low frequencies correspond gentler spectral decreases at high frequencies. Note also that the number of flares increases with decreasing spectral maximum and maximum radio flux. Most of the events

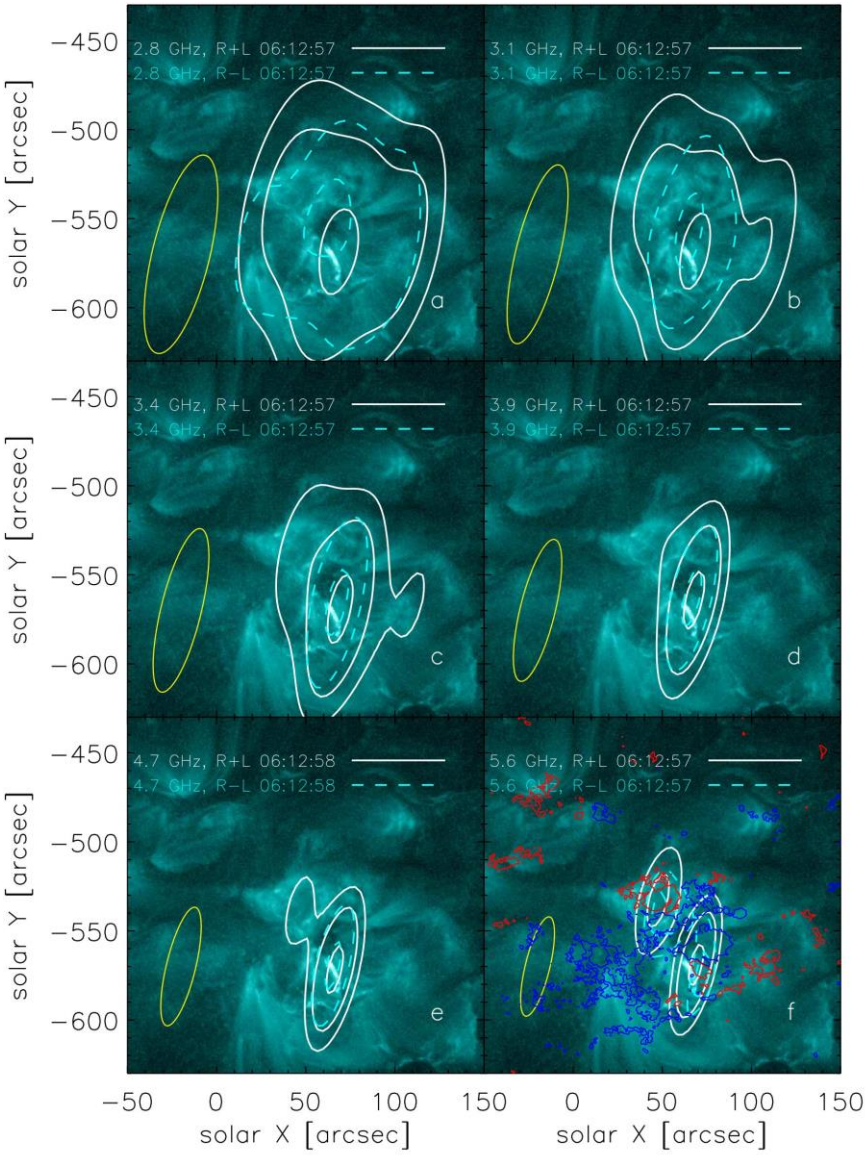

Figure 7. September 25, 2021 event. Images of a flare region at 2.8–5.6 GHz. The background is an AIA/SDO image at 131 Å. White contours are brightness temperatures of radio sources (R+L) at 0.3, 0.5, and 0.9 levels of the maximum value in the image. Dashed blue lines contour circularly-polarized components (R–L) at 0.5 and 0.9 levels. Yellow ovals in the bottom left corner are SRH diagrams at this frequency. Red/blue contours in panel *f* are isolines of the ±200 G longitudinal magnetic field

events in the sample correspond to a non-thermal component, where β=–3.5÷–1.5. The low-frequency spectral slope α has a wide spread of values from 1 to 4 and higher with an expected spread of values for a uniform source from 2.67 to 3.1.

In Table and Figure 6, *c*, the two events (No. 22, 28) in the direction of both low and high frequencies are distinguished by abnormally steep spectral slopes that cannot be attributed to gyrosynchrotron emission even from a uniform source. The spectra for three time points in event No. 22 are displayed in Figure 3. After the narrowband peak shown by the solid curve, spectra become broadband during sub-peaks. Spectra of the sub-peaks can be explained by the gyrosynchrotron emission from a uniform source with the size of the loop observed in EUV emission. The results of calculations performed using the program [Fleishman, Kuznetsov, 2010] are shown by dotted and dashed lines. The best fitting results were obtained when the magnetic field in the source was 180 G, the concentration of radiating non-thermal particles was $1.1 \cdot 10^6$ cm^{-3} during the first sub-peak and $0.8 \cdot 10^6$ cm^{-3} during the second. In both cases, the index of the power-law spectrum of accelerated particles was ~4.4; and the concentration of background plasma, $4 \cdot 10^{10}$ cm^{-3}. The latter value is close to an independent estimate obtained from calculations of the UV emission measure. With such parameters, the shape of the spectra can be significantly affected by the Razin effect since the critical Razin frequency calculated from the obtained values of magnetic field and plasma density $f_R \approx 4.4$ GHz is close to the frequency of maxima of the approximated sub-peak spectra.

At maximum of burst No. 22, the emission band is so narrow that it is impossible to explain it by the gyrosynchrotron emission, including when using the magnetic field intensity and the concentration of background plasma of the gyrosynchrotron source of the sub-peaks obtained above. From the analysis of images of the flare region at 3.9 and 4.2 GHz it follows that a coherent source should also be located in a flare loop, and its size should be slightly smaller than the size of the source at other SRH receiving frequencies.

The theory of coherent narrowband emission mechanisms has been developed in [Zaitsev, Stepanov, 1983; Zaitsev et al., 1997]. It has been shown that when accelerated electrons are injected into a flare loop, along the loop during characteristic transit time the pitch-angular distribution of electrons can be established which generates plasma waves at the upper hybrid frequency. This means that at a plasma density of $4 \cdot 10^{10}$ cm^{-3}, the frequency of the second harmonic is 3.7 GHz, which is close enough to the observed frequency of 4.27 GHz. Emission generation stops when angular anisotropy of accelerated electrons decreases due to interaction with excited turbulence. The frequency of electromagnetic emission generated due to coalescence of plasma waves becomes close to the doubled upper hybrid frequency, and the circular polarization degree should be ~50 %. Recall that polarization of the burst at 3.9 and 4.7 GHz was higher than 60 %.

Thus, the observations of peak emission during the September 25 burst are consistent with the theory [Zaitsev, Stepanov, 1983; Zaitsev et al., 1997]. Note that a similar case with narrowband emission at ~6 GHz has recently been analyzed in [Altyntsev et al., 2022; Altyntsev et al., 2023].

CONCLUSION

BBMS observations allowed us to measure parameters of microwave emission spectra for 30 weak solar flares with an increase in X-rays from A to C1.5. The microwave spectra suggest that in most events plasma heating is accompanied by the appearance of nonthermal electron fluxes, which can be detected as bursts of microwave emission. The burst amplitude dependence of a soft X-ray increase is weakly manifested, i.e. at the same increase, gyrosynchrotron bursts differing by an order of magnitude can occur. The range of low-frequency spectrum growth indices f^{α} can be widely realized α=0.3÷15. The spectrum shape can be significantly influenced by the Razin effect, especially if bursts are generated in dense plasma with relatively weak magnetic fields.

In some cases, the appearance of non-thermal electrons leads to the generation of narrowband bursts at frequencies near the double plasma frequency.

We acknowledge the financial support provided by Russian Science Foundation (RSF) (Grant No. 22-22-00019) and thank the SRH and SDO teams for free access to data. The results were obtained using the Unique Scientific Facility "Siberian Solar Radio Telescope" [http://ckp-rf.ru/usu/73606/] and the equipment of Shared Equipment Center “Angara” [http://ckp-angara.iszf.irk.ru/].

REFERENCES

Altyntsev A.T., Meshalkina N.S., Fedotova A.Ya., Myshyakov I.I. Background microwave emission and microflares in young active region 12635. *Astrophys. J.* 2020a, vol. 905, iss. 2. P. 149. DOI: 10.3847/1538-4357/abc54f.

Altyntsev A., Lesovoi S., Globa M., Gubin A., Kochanov A., Grechnev V., Ivanov E., Kobets V., Meshalkina N., et al. Multiwave Siberian Radioheliograph. *Solar-Terr. Phys.* 2020b, vol. 6, iss. 2, p. 30. DOI: 10.12737/stp-62202003.

Altyntsev A., Meshalkina N., Myshyakov I. Coherent microwave emission as an indicator of non-thermal energy release at a coronal X-ray point. *Solar-Terr. Phys.* 2022, vol. 8, iss. 2, p. 3. DOI: 10.12737/stp-82202201.

Altyntsev A.T., Reid H., Meshalkina N.S., Myshyakov I.I., Zhdanov D.A. Temporal and spatial association between microwaves and type III bursts in the upper corona. *Astronomy and Astrophysics.* 2023, vol. 671, id. A30, p. 7. DOI: 10.1051/0004-6361/202244599.

Battaglia M., Sharma R., Luo Y., Chen B., Yu S., Krucker S. Multiple electron ecceleration instances during a series of solar microflares observed simultaneously at X-rays and microwaves. *Astrophys. J.* 2021, vol. 922, no. 2, p. 134. DOI: 10.3847/1538-4357/ac2aa6.

Berghmans D., Auchère F., Long D.M., Soubrié E., Mierla M., Zhukov A.N., Schühle U., Antolin P., Harra L., et al. Extreme-UV quiet Sun brightenings observed by the Solar Orbiter/EUI. *Astronomy and Astrophysics.* 2021, vol. 656, no. L4. DOI: 10.1051/0004-6361/202140380.

Bogachev S.A., Ulyanov A.S., Kirichenko A.S. Microflares and nanoflares in the solar corona. *Physics – Uspekhi*. 2020, vol. 63, iss. 8, p.783. DOI: 10.3367/UFNe.2019.06.038769.

Chiuderi Drago F., Alissandrakis C., Hagyard M. Microwave emission above steady and moving sunspots. *Solar Phys.* 1987, vol. 112, p. 89. DOI: 10.1007/BF00148490.

Dulk G.A., Marsh K.A. Simplified expressions for the gyrosynchrotron radiation from mildly relativistic, nonthermal and thermal electrons. *Astrophys. J.* 1982, vol. 259, p. 350. DOI: 10.1086/160171.

Fleishman G.D., Kuznetsov A.A. Fast gyrosynchrotron codes. *Astrophys. J.* 2010, vol. 721, iss. 2, p. 1127. DOI: 10.1088/0004-637X/721/2/1127.

Gary D.E., Hurford G.E. Multifrequency observations of a solar microwave burst with two-dimensional spatial resolution. *Astrophys. J.* 1990, vol. 361, p. 290. DOI: 10.1086/169194.

Gary D.E., Hartl M.D., Shimizu T. Nonthermal radio emission from solar soft X-ray transient brightenings. *Astrophys. J.* 1997, vol. 477, p. 958. DOI: 10.1086/303748.

Ginzburg V.L., Syrovatskii S.I. Cosmic Magnetobremsstrahlung (Synchrotron Radiation). *Ann. Rev. Astron. Astrophys.* 1965, vol. 3, p. 297. DOI: 10.1146/annurev.aa.03.090165.001501.

Gopalswamy N., Zhang J., Kundu M.R., Schmahl E.J., Lemen J.R. Fast time structure during transient microwave brightenings: evidence for nonthermal processes. *Astrophys. J.* 1997, vol. 491, iss. 2, p. L115. DOI: 10.1086/311063.

Krucker S., Hurford G.J., Grimm O. The Spectrometer/Telescope for Imaging X-rays (STIX). *Astronomy and Astrophysics.* 2020, vol. 642, p. A15. DOI: 10.1051/0004-6361/201937362.

Kundu M.R., Schmahl E.J., Grigis P.C., Garaimov V.I., Shibasaki K. Nobeyama radio heliograph observations of RHESSI microflares. *Astronomy and Astrophysics.* 2006, vol. 451, iss. 2, pp. 691–707.

Li Z., Su Y., Veronig A., Kong S., Gan W., Chen W. Detailed thermal and nonthermal processes in an A-class microflare. *Astrophys. J.* 2022, vol. 930, no. 2, p.147. DOI: 10.3847/1538-4357/ac651c.

Lin R.P., Dennis B.R., Hurford G.J. The Reuven Ramaty High-Energy Solar Spectroscopic Imager. *Solar Phys.* 2002, vol. 210, p. 3. DOI: 10.1023/A:1022428818870.

Lysenko A., Altyntsev A., Meshalkina N., Zhdanov D., Fleishman G. Statistics of "cold" early impulsive solar flares in x-ray and microwave domains. *Astrophys. J.* 2018, vol. 856. DOI: 10.3847/1538-4357/aab271.

Meegan C., Lichti G., Bhat P.N., Bissaldi E., Briggs M.S., Connaughton V., Diehl R., Fishman G., Greiner J., Hoover A.S. The Fermi gamma-ray burst monitor. *Astrophys. J.* 2009, vol. 702, p. 791. DOI: 10.1088/0004-637X/702/1/791.

Muratov A.A. 2-24 GHz Solar Spectropolarimeter. *Baikal Young Scientists' International School on Fundamental Physics. XII Young Scientists' Conference "Interaction Of Fields And Radiation With Matter"*. 2011, pp. 21–22. (In Russian).

Neupert W.M. Comparison of Solar X-ray line emission with microwave emission during flares. *Astrophys. J.* 1968, vol. 153, p. L59. DOI: 10.1086/180220.

Nindos A., Kundu M.R., White S.M., Gary D.E., Shibasaki K., Dere K.P. Microwave and extreme ultraviolet observations of solar polar regions. *Astrophys. J.* 1999, vol. 527, iss. 1, pp. 415–425.

Nita G.M., Gary D.E., Lee J. Statistical study of two years of solar flare radio spectra obtained with the Owens Valley Solar Array. *Astrophys. J.* 2004, vol. 605, iss. 1, pp. 528–545.

Qiu J., Liu Ch., Gary D.E., Nita G.M., Wang H. Hard X-Ray and Microwave Observations of Microflares. *Astrophys. J.*. 2004, vol. 612, no. 1, p. 530. DOI: 10.1086/422401.

Ramaty R. Gyrosynchrotron emission and absorption in a magnetoactive plasma. *Astrophys. J.* 1969, vol. 158, p. 753. DOI: 10.1086/150235.

Raulin J.-P., White S.M., Kundu M.R., Silva A.V.R., Shibasaki K. Multiple components in the millimeter emission of a solar flare. *Astrophys. J.* 1999, vol. 522, iss. 1, pp. 547–558.

Schadee A., de Jager C., Svestka Z. Enhanced X-ray emission above 3.5 keV in active regions in the absence of flares. *Solar Phys.* 1983, vol. 89, p. 287. DOI: 10.1007/BF00217252.

Shaik S.B., Gary D.E. Implications of flat optically thick microwave spectra in solar flares for source size and morphology. *Astrophys. J.* 2021, vol. 919, p. 44. DOI: 10.3847/1538-4357/ac0fdb.

Shibasaki K., Chiuderi-Drago F., Melozzi M., Slottje C., Antonucci E. Microwave, ultraviolet, and soft X-ray observations of hale region 16898. *Solar Phys*. 1983, vol. 89, p. 307. DOI: 10.1007/BF00217253.

Stahli M., Gary D.E., Hurford G.J. High-resolution microwave spectra of solar bursts. *Solar Phys.* 1989, vol. 120, p. 351. DOI: 10.1007/BF00159884.

Stoiser S., Veronig A.M., Aurass H., Hanslmeier A. RHESSI microflares: I. X-ray properties and multiwavelength characteristics. *Solar Phys.* 2007, vol. 246, iss. 2, p. 339.

Zaitsev V.V., Kruger A., Hildebrandt J., Kliem B. Plasma radiation of power-law electrons in magnetic loops: Application to solar decimeter-wave continua. *Astronomy and Astrophysics.* 1997, vol. 328, p. 390.

Zaitsev V.V., Stepanov A.V. The plasma radiation of flare kernels. *Solar Phys.* 1983, vol. 88, p. 297. DOI: 10.1007/BF00196194.

Zhdanov D.A., Zandanov V.G. Broadband microwave spectropolarimeter. *Central European Astrophys. Bull.* 2011, vol. 35, p. 223.

Zhdanov D.A., Zandanov V.G. Observations of microwave fine structures by the Badary broadband microwave spectropolarimeter and the Siberian Solar Radio Telescope. *Solar Phys*. 2015, vol. 290, iss. 1, p. 287. DOI: 10.1007/ s11207-014-0553-3.

Xiao H., Maloney S., Krucker S., Dickson E., Massa P., Lastufka E., et al. The data center for the Spectrometer and Telescope for Imaging X-rays (STIX) onboard Solar Orbiter. 2023, https://arxiv.org/abs/2302.00497.

URL: http://ckp-rf.ru/usu/73606/ (accessed August 24, 2023).

URL: http://ckp-angara.iszf.irk.ru (accessed August 24, 2023).

This paper is based on material presented at the 18th Annual Conference on Plasma Physics in the Solar System, February 6–10, 2023, IKI RAS, Moscow.

Original Russian version: Zhdanov D.A., Altyntsev A.T., Meshalkina N.S., Anfinogentov S.A., published in Solnechno-zemnaya fizika. 2023. Vol. 9. Iss. 3. P. 111–121. DOI: 10.12737/szf-93202312.

How to cite this article

Zhdanov D.A., Altyntsev A.T., Meshalkina N.S., Anfinogentov S.A. Statistical analysis of microflares as observed by the 4–8 GHz spectropolarimeter. *Solar-Terrestrial Physics*. 2023. Vol. 9. Iss. 3. P. 102–111. DOI: 10.12737/stp-93202312.